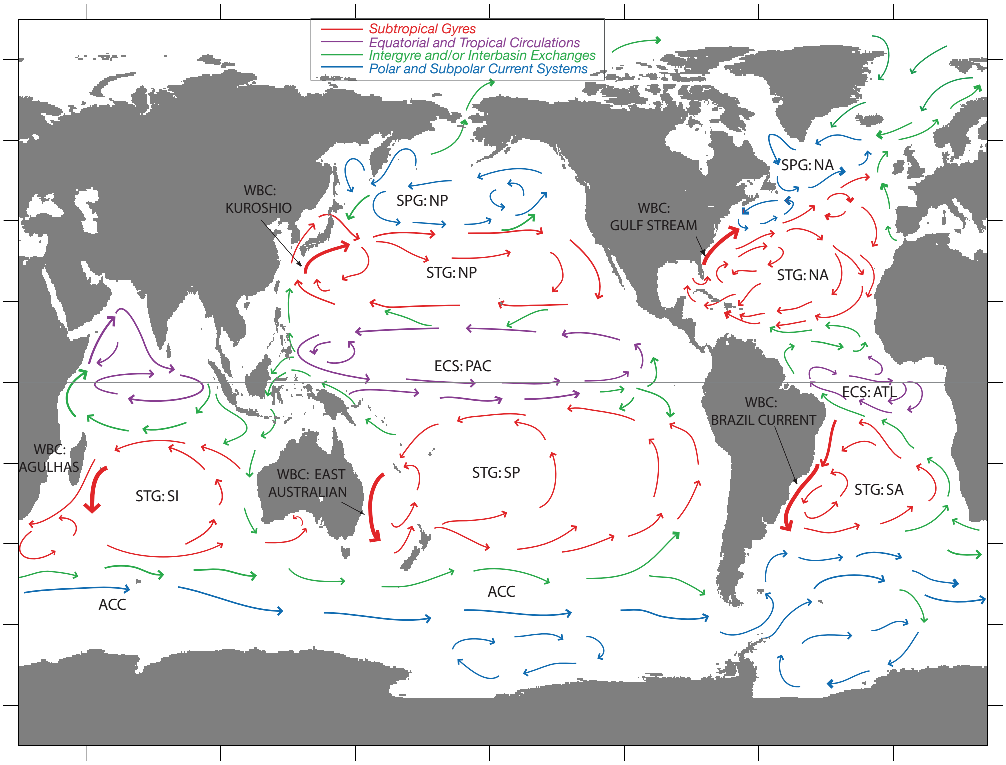

Fig. 14.1 A schema of the main currents of the global ocean. Key: STG – SubTropical Gyre; SPG – SubPolar Gyre; WBC – Western Boundary Current; ECS – Equatorial Current System; NA – North Atlantic; SA – South Atlantic; NP – North Pacific; SP – South Pacific; SI – South Indian; ACC – Antarctic Circumpolar Current; ATL – Atlantic; PAC – Pacific. The figure is a qualitative, and not quantitative, representation of the actual flow.

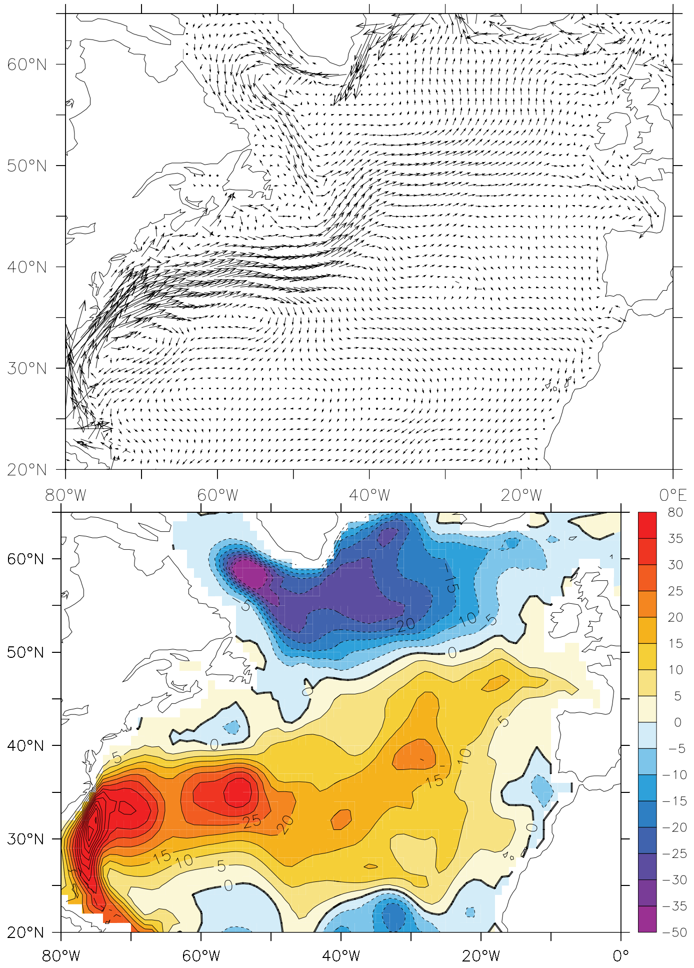

Fig. 14.2 Top: the time averaged velocity field at a depth of 75 m in the North Atlantic, obtained by constraining a numerical model to observations. Bottom: the streamfunction of the vertically integrated flow, in Sverdrups ($1\,\mathrm{Sv} = 10^9\,\mathrm{kg\,s^{-1}}$). Note the presence of an anticyclonic subtropical gyre, a cyclonic subpolar gyre, and intense western boundary currents.[1]

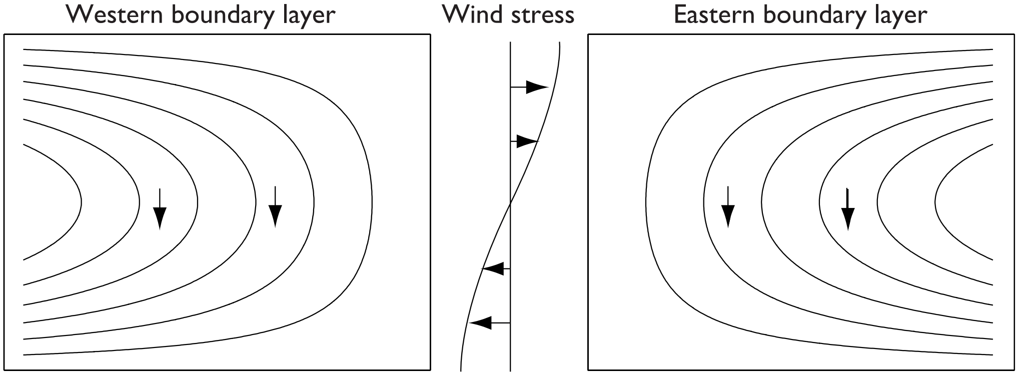

Fig. 14.3 Two possible Sverdrup flows, ψ_I, for the wind stress shown in the centre. Each solution satisfies the no-flow condition at either the eastern or western boundary, and a boundary layer is therefore required at the other boundary. Both flows have the same, equatorward, meridional flow in the interior. Only the flow with the western boundary current is physically realizable, however, because only then can friction produce a curl that opposes that of the wind stress, so allowing the flow to equilibrate.

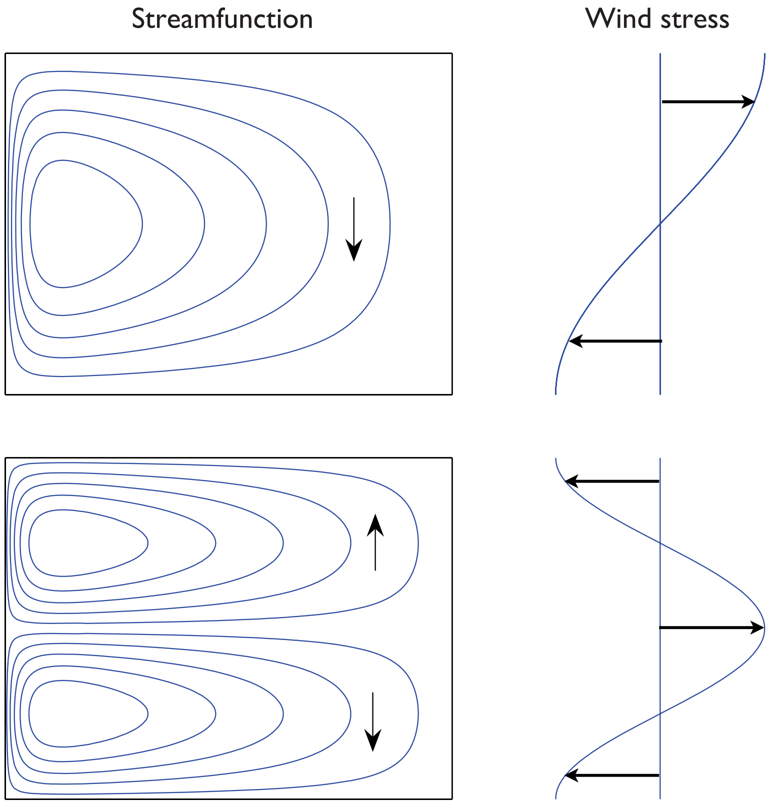

Fig. 14.4 Two solutions of the Stommel model. Upper panel shows the streamfunction of a single-gyre solution, with a wind stress proportional to $-\cos(\pi y/a)$ (in a domain of side a), and the lower panel shows a two-gyre solution, with wind stress proportional to $\cos(2\pi y/a)$. In both cases $\epsilon_S = 0.04$.

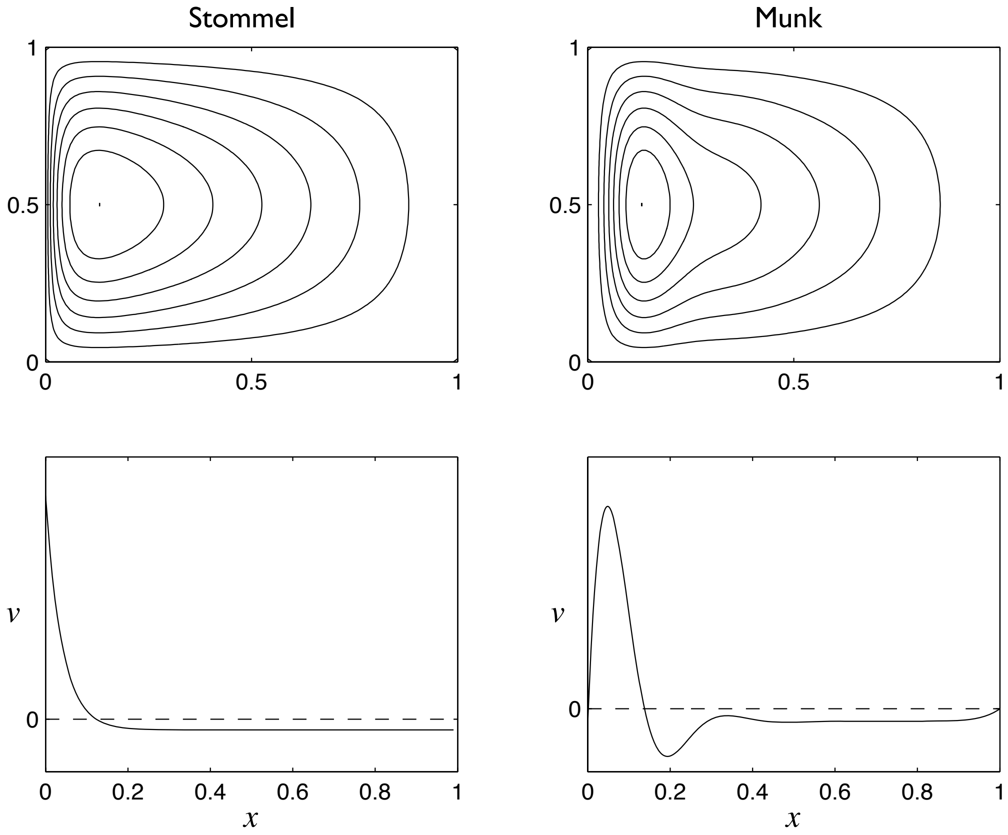

Fig. 14.5 The Stommel and Munk solutions, (14.49) with $\epsilon_S = \epsilon_M^{1/3} = 0.04$, with the wind stress $\tau = -\cos \pi y$, for $x, y \in (0, 1)$. Upper panels are contours of streamfunction in the x-y plane, and the flow is clockwise. The lower panels are plots of meridional velocity, v, as a function of x, in the centre of the domain ($y = 0.5$). The Munk solution can satisfy both no-normal flow and one other boundary condition at each wall, here chosen to be no-slip.

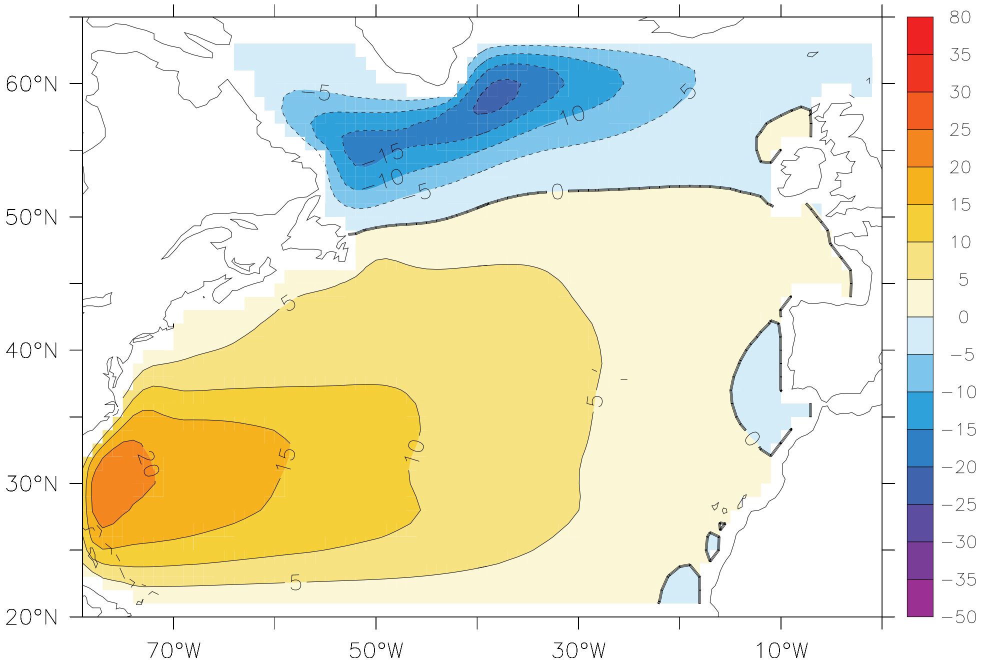

Fig. 14.6 The solution (streamfunction, in Sverdrups) to the Stommel–Munk problem numerically calculated for the North Atlantic, using the observed wind field. The model ocean has realistic geometry, but is flat-bottomed. The calculation qualitatively reproduces the large-scale patterns, including the subtropical and subpolar gyre and the western intensification of both, although the separation of the Gulf Stream from the coast is a little too far North. Compare with Fig. 14.2.[2]

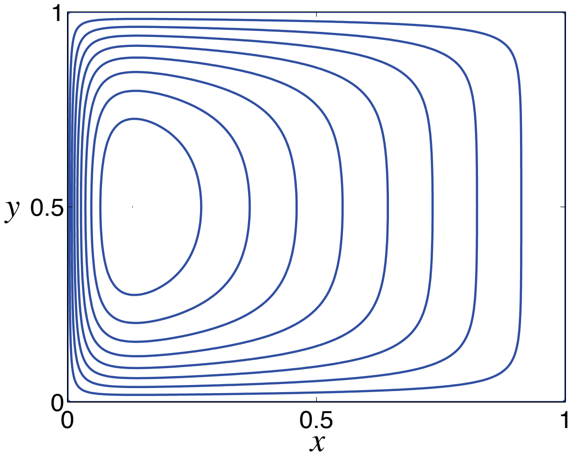

Fig. 14.7 Solutions to the Stommel problem with a wind stress that increases linearly from $y = 0$ to $y = 1$, as in (14.50). The interior solution is $\psi_I = (1 - x)$, or $v_I = -1$, necessitating zonal boundary layers at $y = 0$ and $y = 1$, as well as a western boundary layer at $x = 0$.

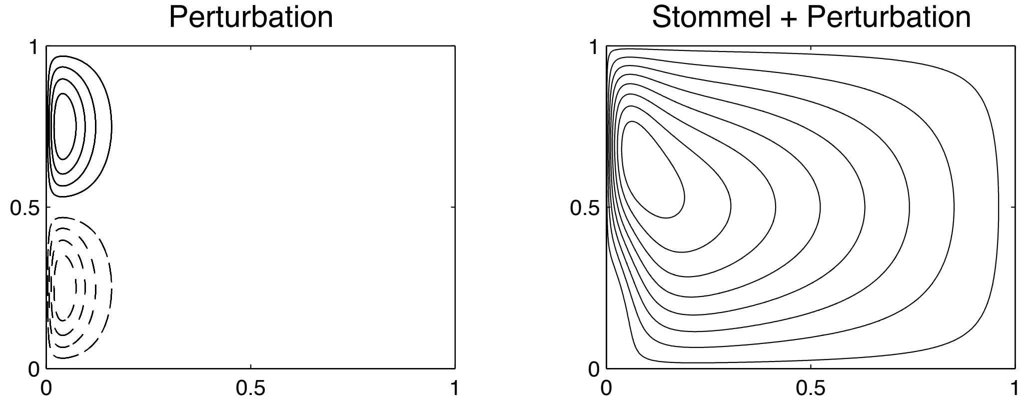

Fig. 14.8 The nonlinear perturbation solution of the Stommel problem, calculated according to (14.63). On the left is the perturbation, $-R_\beta \pi^3/(2\epsilon_S^2)\sin(2\pi y)xe^{-x/\epsilon_S}$, and on the right is the reconstituted solution, using $R_\beta = 10^{-4}$ and $\epsilon = 0.04$. Dashed contours are negative.

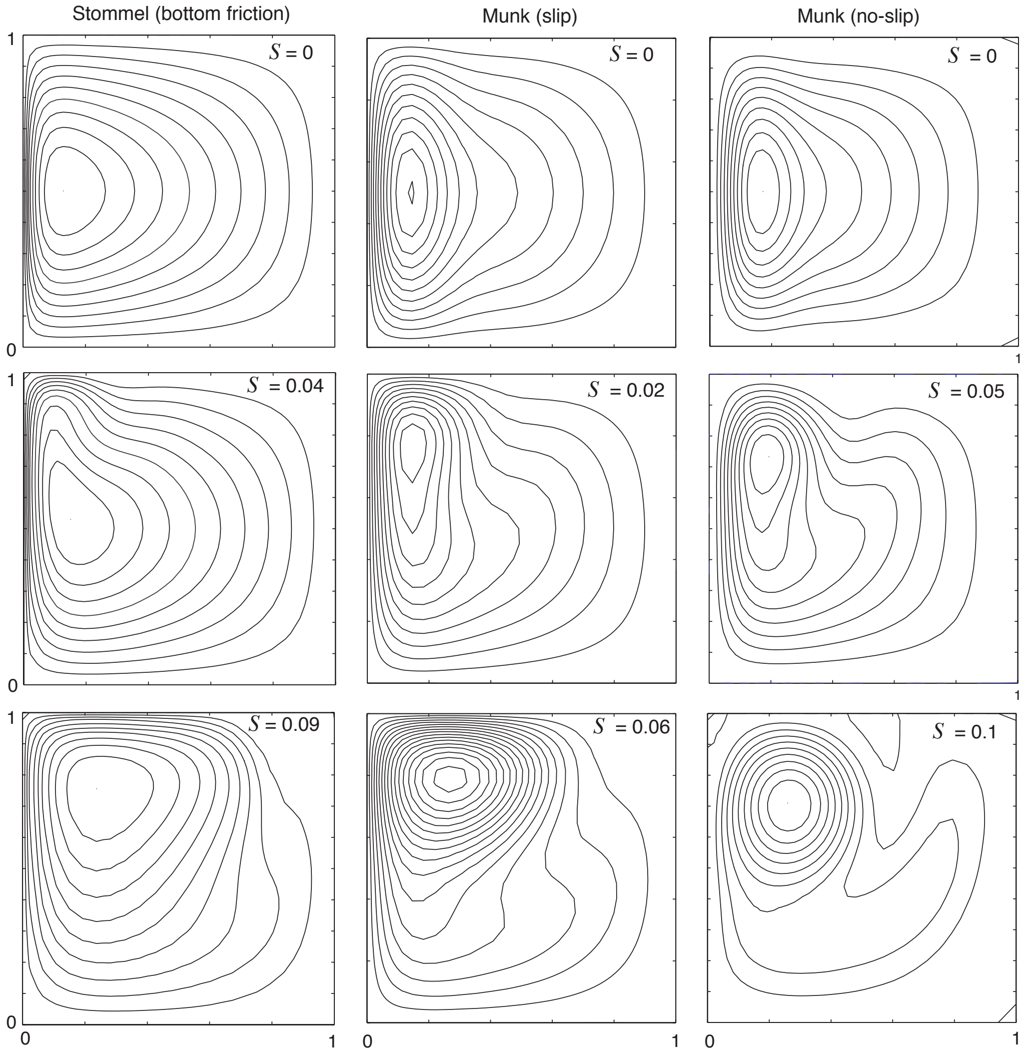

Fig. 14.9 Streamfunctions in solutions of the nonlinear Stommel and Munk problems, obtained numerically with a Newton's method, for various values of the nonlinearity parameter $S = R_\beta^{1/2}$. As in the perturbation solution, for small values of nonlinearity the centre of the gyre moves polewards, strengthening the boundary current in the north-western quadrant (for a northern-hemisphere solution). As nonlinearity increases, the recirculation of the gyre dominates, and the solutions become increasingly inertial.[3]

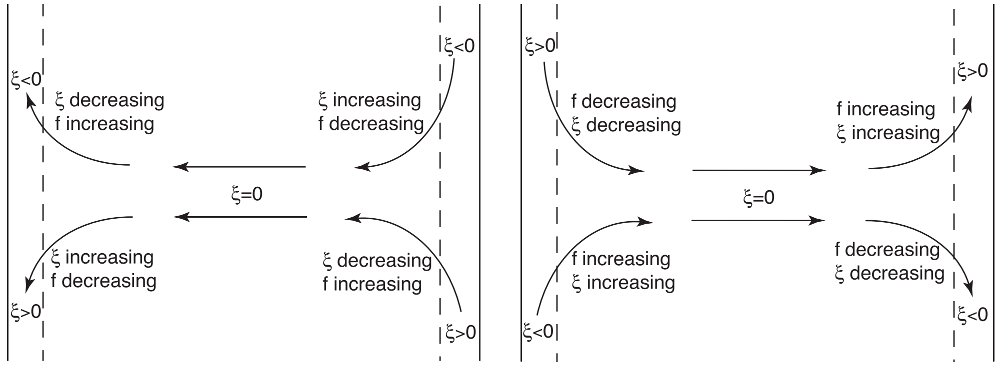

Fig. 14.10 Putative inertial boundary layers connected to a westward flowing internal flow (left panel) or eastward flowing internal flow (right panel), in the Northern Hemisphere. Westward flow into the western boundary layer, or flow emerging from an eastern boundary layer, is able to conserve its potential vorticity through a balance between changes in relative vorticity and Coriolis parameter. But flow cannot emerge smoothly from a western boundary layer into an eastward flowing interior and still conserve its potential vorticity. The right panel thus has inconsistent dynamics.

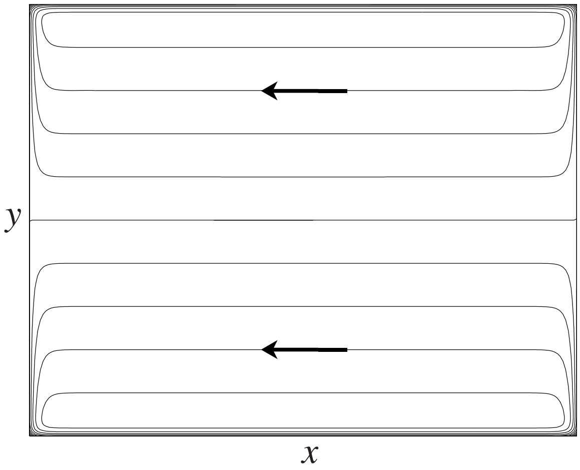

Fig. 14.11 The Fofonoff solution. Plotted are contours (streamlines) of (14.87) in the plane $0 < x < x_E$, $0 < y < y_N$ with $U = 1$, $y_N = 1$, $x_E = y_N = 1$, $y_0 = 0.5$ and $\delta_I = 0.05$. The interior flow is westward everywhere, and $\psi = 0$ at $y = y_0$. In addition, boundary layers of thickness $\delta_I = \sqrt{U/\beta}$ bring the solution to zero at $x = (0, x_E)$ and $y = (0, y_N)$, excepting small regions at the corners.

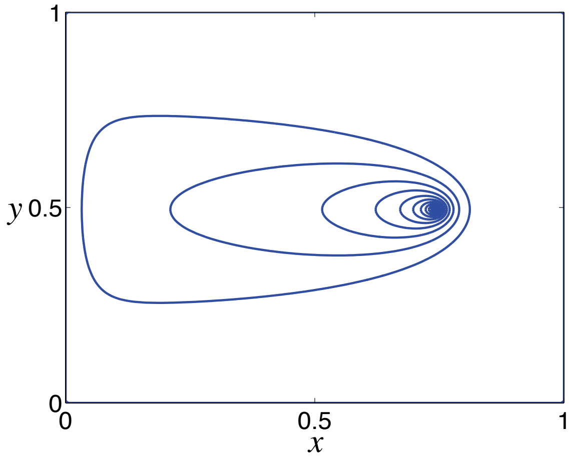

Fig. 14.12 The β-plume, namely Green's function for the Stommel problem. Specifically we plot the solution of (14.93) with $\psi = 0$ at the walls, and a delta-function source at $x = 0.75$, $y = 0.5$. The streamfunction trails westward from the source, as if it were a tracer being diffused while being advected westward along lines of constant f.

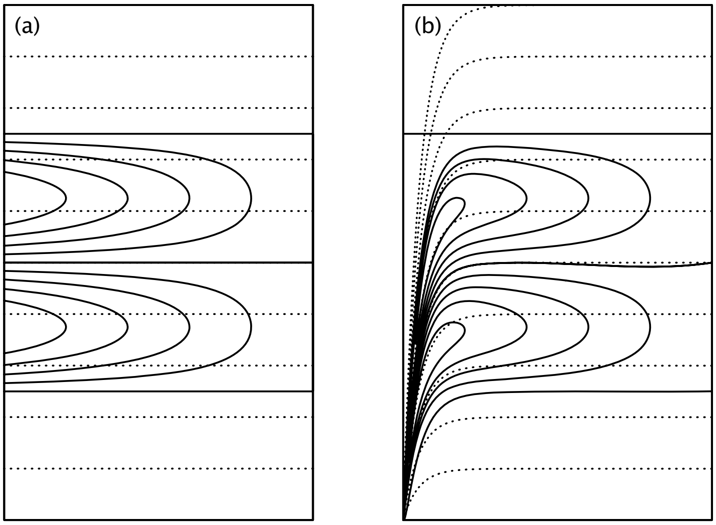

Fig. 14.13 The two-gyre Sverdrup flow (solid contours) for (a) a flat-bottomed domain and (b) a domain with sloping sidewalls. The f/h contours are dotted.[4]

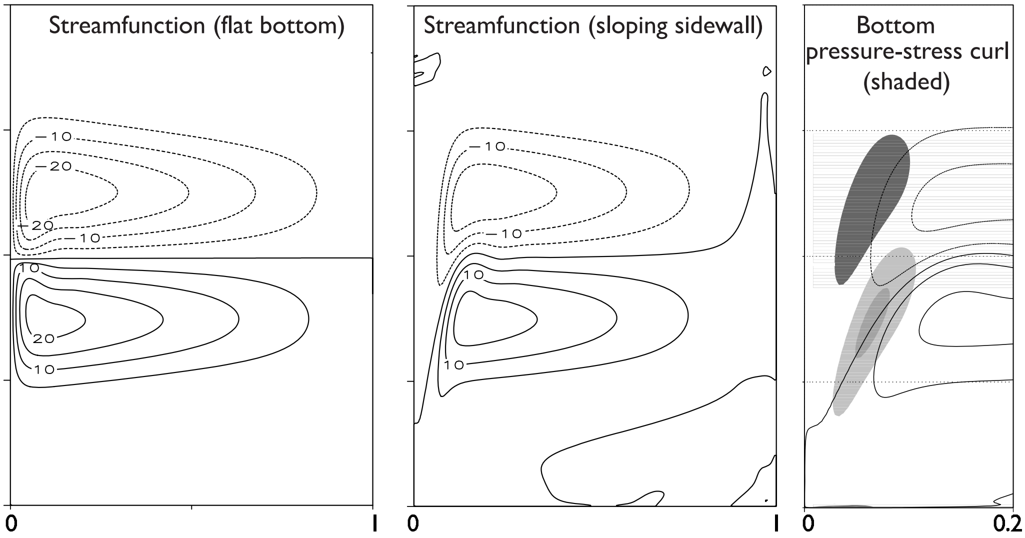

Fig. 14.14 The numerically obtained steady solution to the homogenous problem with a two-gyre forcing and friction, for a flat-bottomed doman and a domain with sloping western sidewall. The shaded regions in the right panel show the regions where bottom pressure-stress curl is important, in the meridional flow of the western boundary currents.[5]

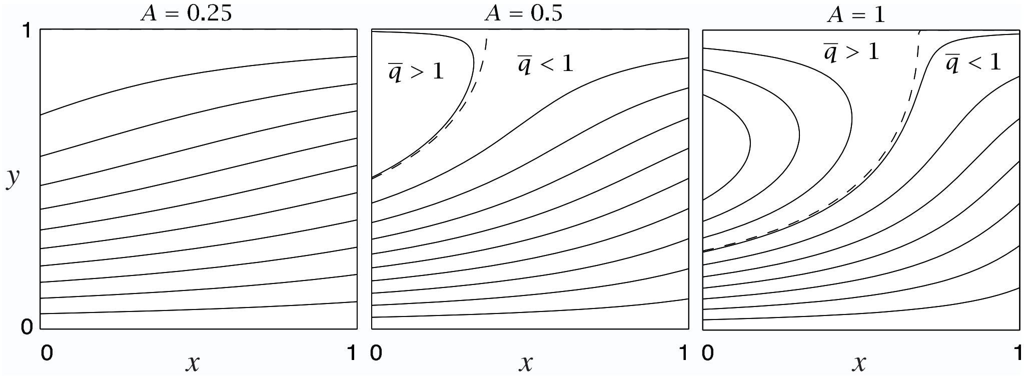

Fig. 14.15 Contours of $\overline{q} = \beta y + A \sin \pi y(1 - x)$, with $\beta = 1$. The dashed line is $\overline{q} = 1$, which separates the blocked region to the east ($\overline{q} < 1$) from the closed region to the west ($\overline{q} > 1$). See Fig. 14.16 for plots of the other fields.

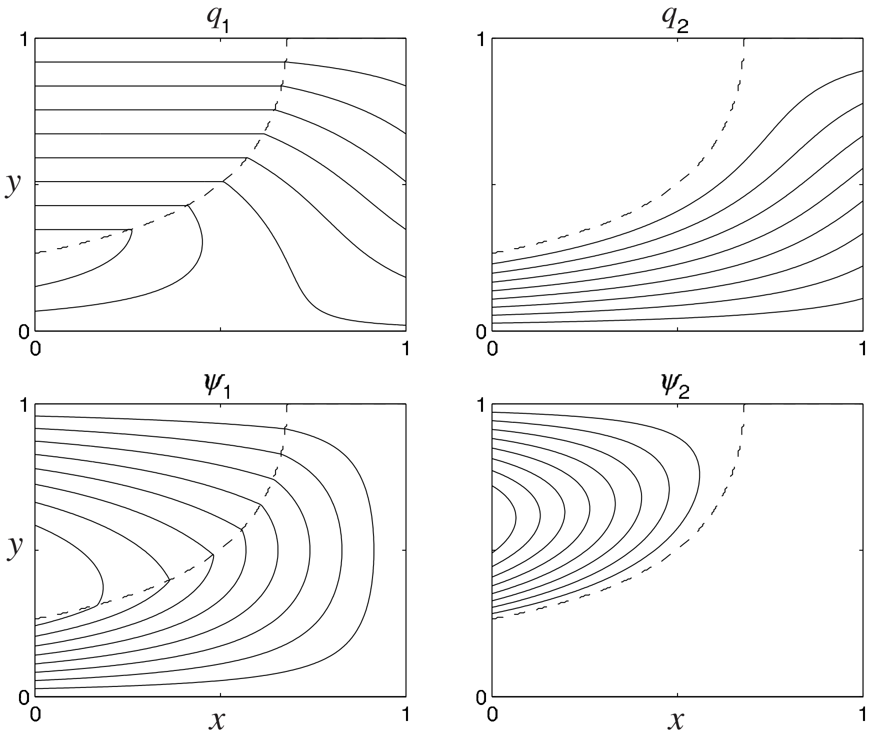

Fig. 14.16 Upper- and lower-level potential vorticity and streamfunction for the canonical wind stress (14.111). The field of $\overline{q}$ is that of Fig. 14.15 with $A = 1$. The dashed line divides the blocked region from the closed region. The lower layer streamfunction ψ_2 is non-zero only in the closed region, and here $q_2 = \beta L$ and $q_1 = 2\beta y - \beta L$. In the blocked region the upper layer carries all of the Sverdrup transport. Both the streamfunction and potential vorticity are continuous at the divide: $\psi_2 = 0$ and $q_2 = \overline{q} = \beta L$.

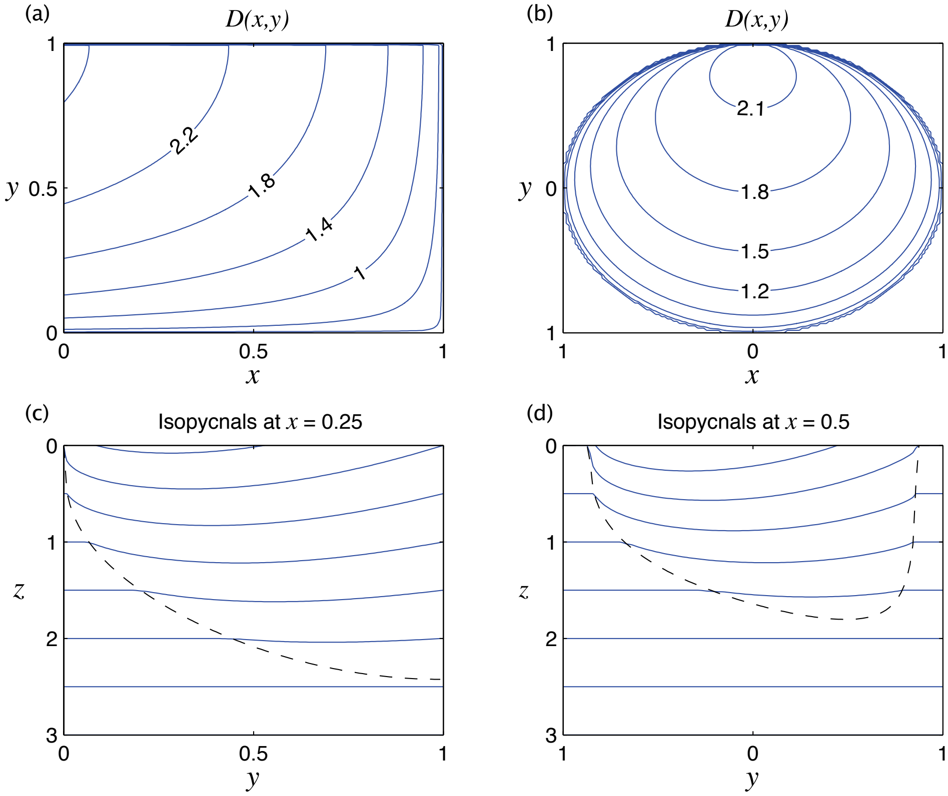

Fig. 14.17 Solutions of (14.112) for two different barotropic streamfunctions. On the left $\psi_B = (1 - x)\sin \pi y$ and on the right $\psi_B = 1 - (x^2 + y^2)$ for $x^2 + y^2 < 1$, zero elsewhere. The upper panels show contours of the depth of the wind-influenced region [solutions of (14.145)]. The depth increases to the northwest in the left panel, and to the north in the right panel, so that in both cases the area of the bowl shrinks with depth. The lower panels are contours of $z + (\beta L/f_0)\psi_z/2$, with $\beta L/f_0 = 1/2$, obtained from (14.141) or (14.146), at $x = 0.25$ and $x = -0.5$ in the two cases. These are isopcynal surfaces, with a rather large value of $\beta L/f_0$ to exaggerate the displacement in the bowl region. The dashed lines indicate the boundary of the bowl region, outside of which the isopycnals are flat.

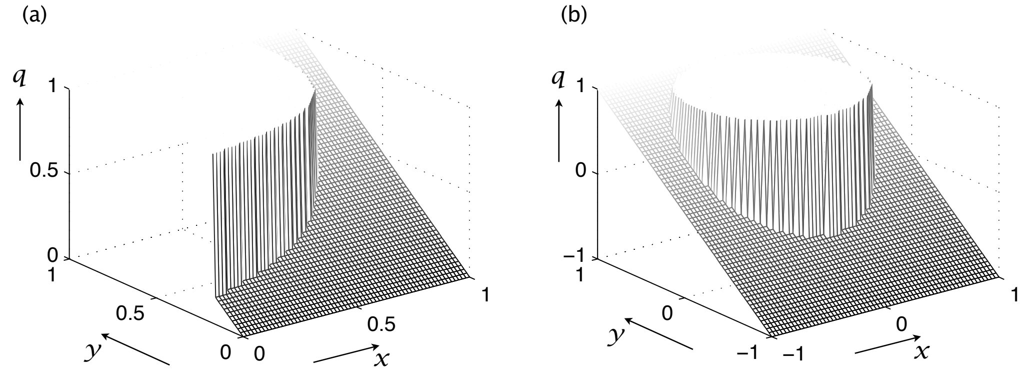

Fig. 14.18 As for Fig. 14.17, but now a perspective of potential vorticity [obtained from (14.147)]. Within the bowls the circulation is clockwise and the potential vorticity is uniform. Outside the bowls the fluid is stationary and the potential vorticity has the planetary value βy. The value of potential vorticity within the bowl is the planetary value at the poleward edge of the gyre, and is the same value at all depths.

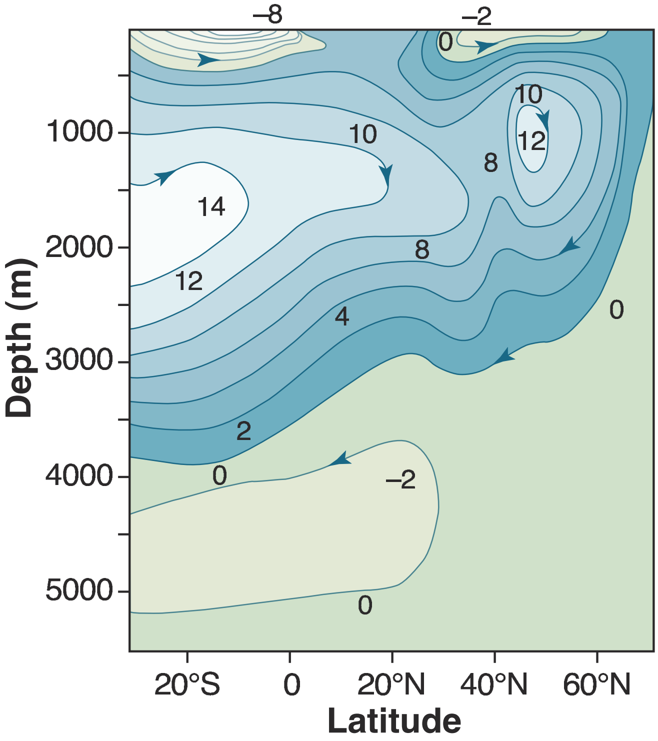

Fig. 15.1 The mean meridional overturning circulation in the North Atlantic, obtained with a combination of observations and a model. The contours are the streamfunction of the zonally averaged meridional flow. The units are Sverdrups, and the circulation is mostly clockwise, with sinking at high latitudes.[1]

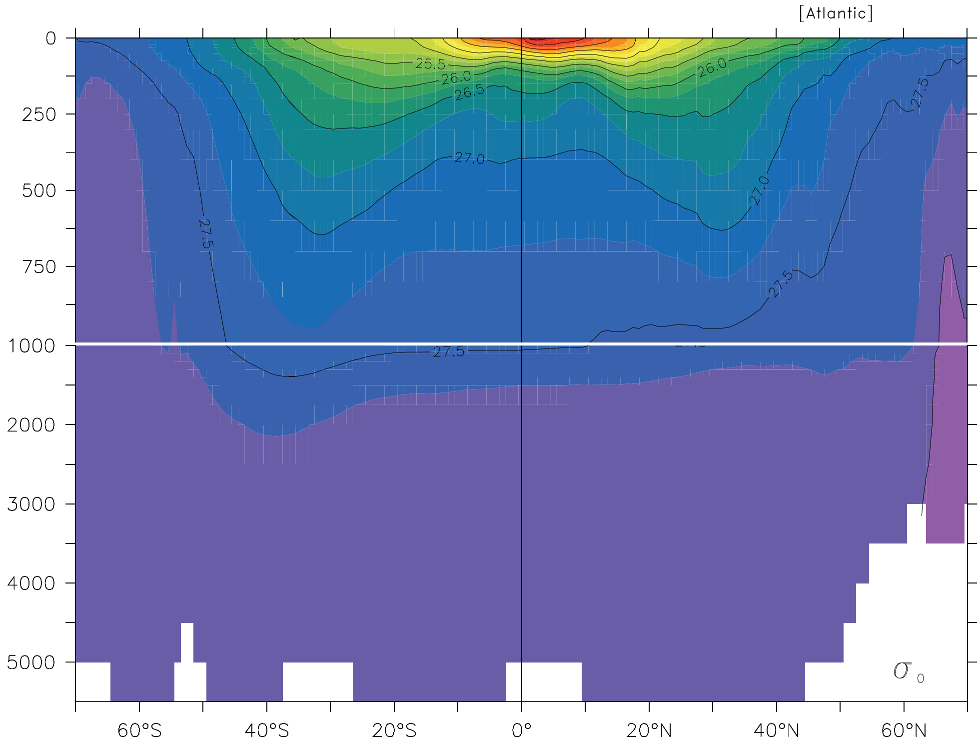

Fig. 15.2 The zonally averaged potential density (σ_θ) in the Atlantic ocean, as a function of depth (m) and latitude. Note the break in the vertical scale at 1000 m. The region of rapid change of density (and temperature) is concentrated in the upper kilometre, in the *main thermocline,* below which the ocean has a much more uniform density.[2]

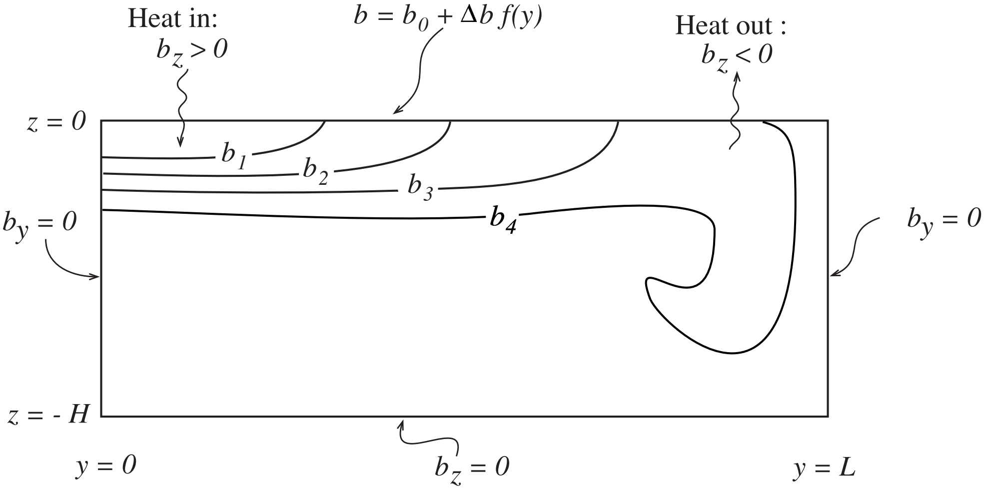

Fig. 15.3 A schema of sideways convection. The fluid is differentially heated and cooled along its top surface, whereas all the other walls are insulating. The result is, typically, a small region of convective instability and sinking near the coldest boundary, with generally upwards motion elsewhere.[3]

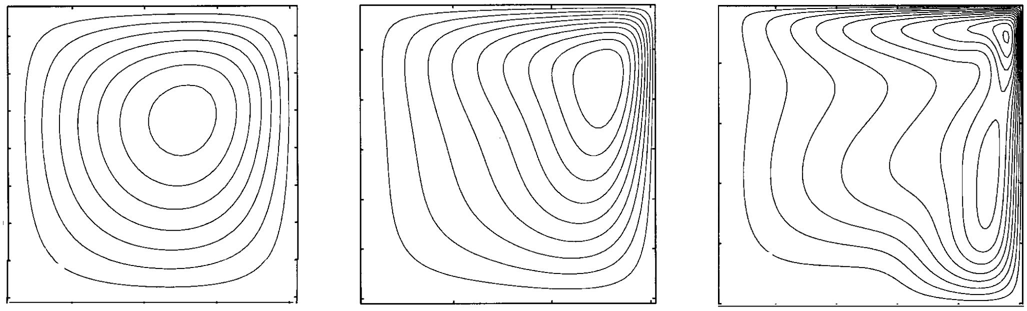

Fig. 15.4 The streamfunction in a numerical simulation of two-dimensional sideways convection.[4] The circulation is clockwise, and the imposed temperature at the top linearly decreases from left to right, and the other walls are insulating. From left to right the Rayleigh numbers are 10^4, 10^6 and 10^8, and the contour interval is 1, 4 and 10 in arbitrary units. The Prandtl number is 10.

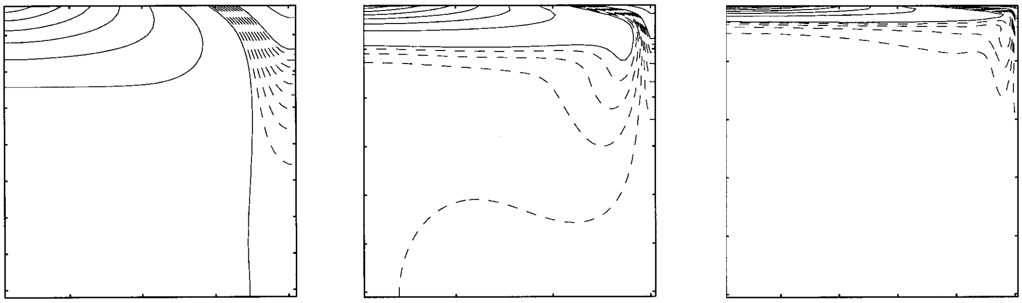

Fig. 15.5 The temperature or buoyancy field corresponding to the streamfunction fields shown in Fig. 15.4. Note an increasingly sharp gradient (a thermocline) near the top as the Rayleigh number increases, and that the bulk of the domain is filled with the densest available fluid.

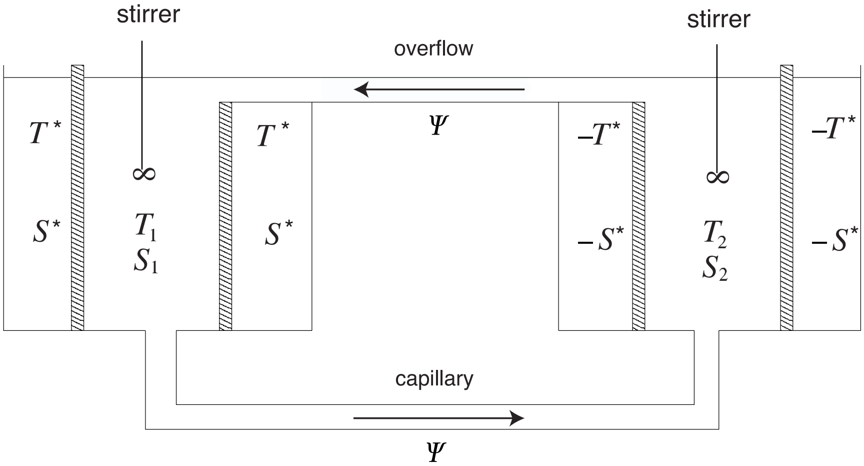

Fig. 15.6 A two-box model of relevance to the overturning circulation of the ocean. The shaded walls are porous, and each box is well mixed by its stirrer. Temperature and salinity evolve by way of fluid exchange between the boxes via the capillary tube and the overflow, and by way of relaxation with the two infinite reservoirs at $(+T^*, +S^*)$ and $(-T^*, -S^*)$.

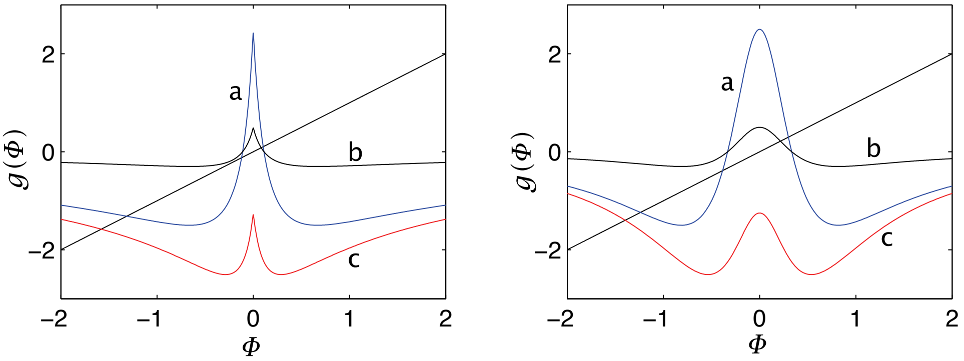

Fig. 15.7 Left panel: graphical solution of the two-box model. The straight line has unit slope and passes through the origin, and the curved lines plot the function $f(\Phi)$ as given by the right-hand side of (15.43). The intercepts of the two are solutions to the equation. The parameters for the three curves are: a, $\gamma = 5$, $\delta = 1/6$, $\mu = 1.5$; b, $\gamma = 1$, $\delta = 1/6$, $\mu = 1.5$; c, $\gamma = 5$, $\delta = 1/6$, $\mu = 0.75$. Right panel: the same except with Φ^2 in place of $|\Phi|$ on the rhs of (15.43).

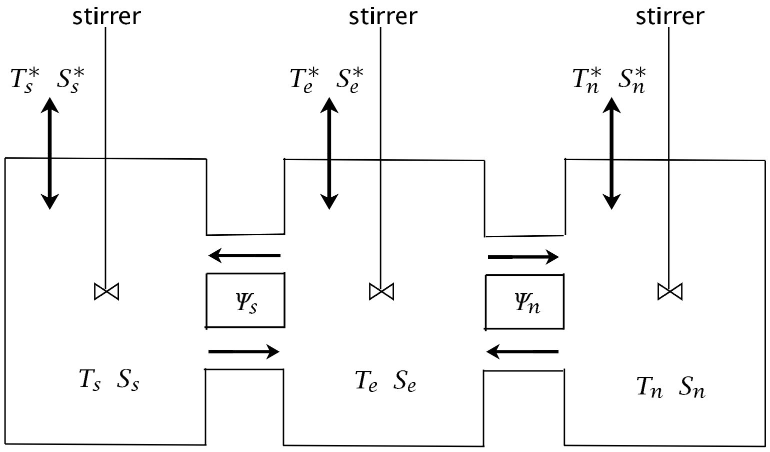

Fig. 15.8 A three-box model. Each box contains fluid with uniform values of temperature and salinity, each exchanges fluid with its neighbour, and in each the temperature and salinity are relaxed toward fixed atmospheric values.

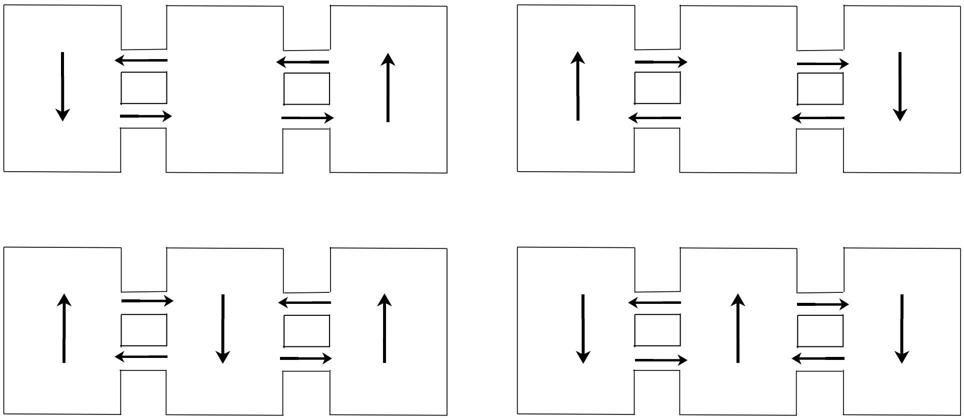

Fig. 15.9 Schematic of four solutions to the three box model with the symmetric forcing $S_s^* = S_n^*$ and $T_n^* = T_s^*$. The two solutions on the top row have an asymmetric, ‘pole-to-pole’, circulation whereas the solutions on the bottom row are symmetric.[5]

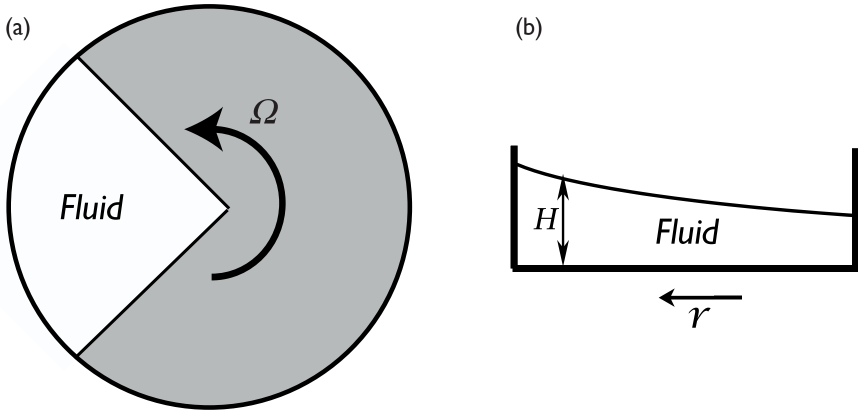

Fig. 15.10 The experimental set-up in the Stommel–Arons–Faller rotating tank experiment. (a) A plan view of the apparatus. The fluid is contained in the sector at left. (b) Side view. The free surface of the fluid slopes up with increasing radius, giving a balance (in the rotating frame) between the centrifugal force pointing outwards and the pressure force pointing inwards. Small pipes may be introduced into the fluid to provide mass sources and sinks.

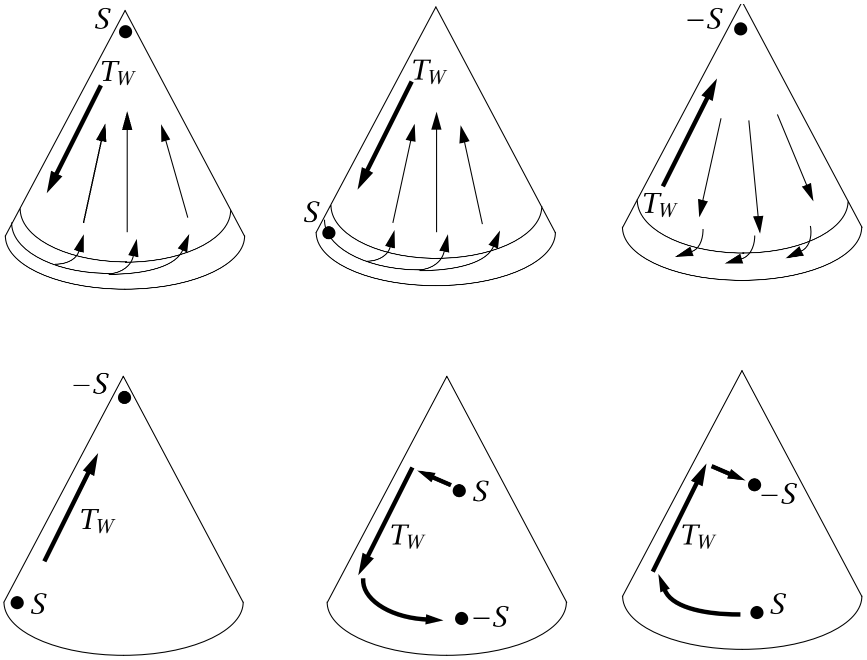

Fig. 15.11 Idealized examples of the flow in the rotating sector experiments, with various locations of a source (S) or sink ($-S$) of mass.

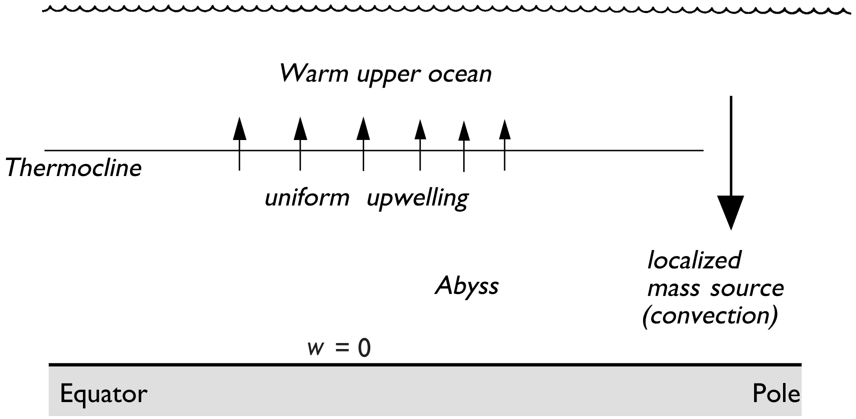

Fig. 15.12 The structure of simple Stommel–Arons ocean model of the abyssal circulation. Convection at high latitudes provides a localized mass-source to the lower layer, and upwelling through the thermocline provides a more uniform mass sink.

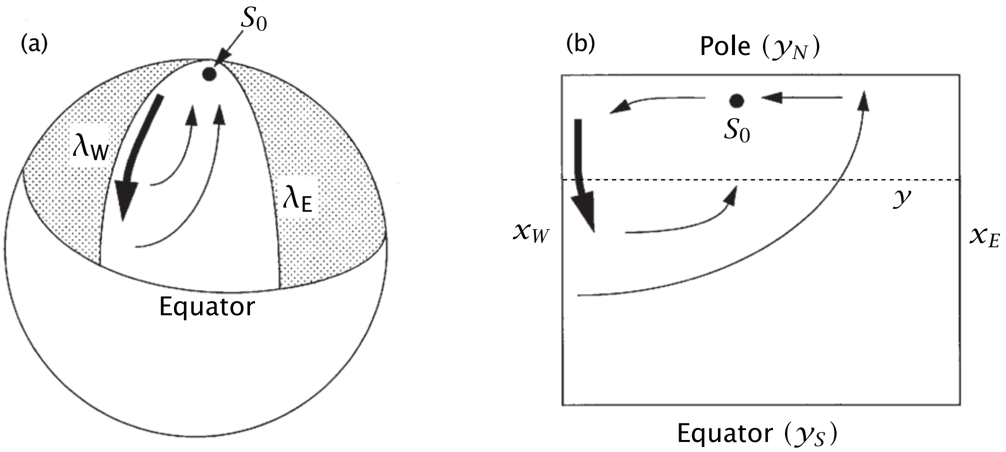

Fig. 15.13 Abyssal circulation in a spherical sector (left) and in a corresponding Cartesian rectangle (right).

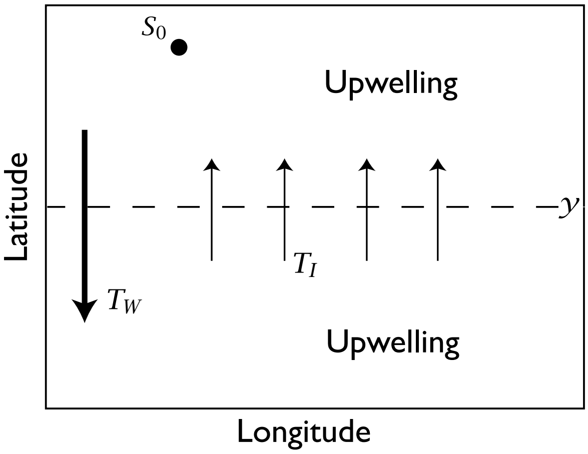

Fig. 15.14 Mass budget in an idealized abyssal ocean. Polewards of some latitude y, the mass source (S_0) plus the polewards mass flux across y (T_I) are equal to the sum of the southwards mass flux in the western boundary current (T_W) and the integrated loss due to upwelling (U) polewards of y. See (15.69).

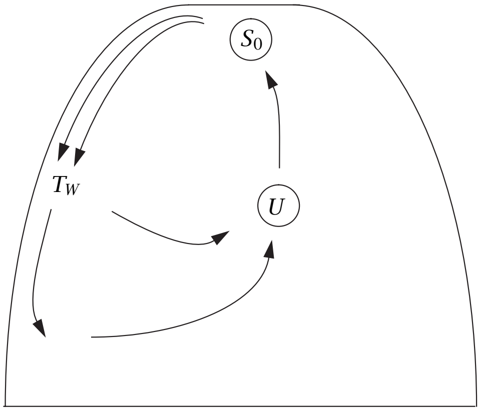

Fig. 15.15 Schematic of a Stommel–Arons circulation in a single sector. The transport of the western boundary current is greater than that provided by the source at the apex, illustrating the property of *recirculation.* The transport in the western boundary current T_W decreases in intensity equatorwards, as it loses mass to the polewards interior flow, and thence to upwelling. The integrated sink, due to upwelling, U, exactly matches the strength of the source, S.

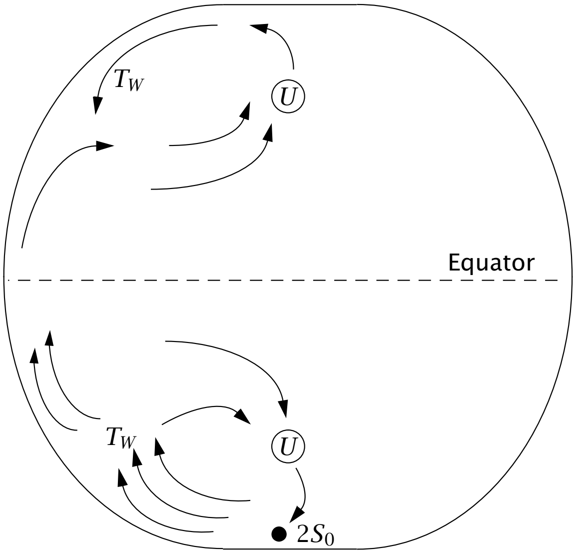

Fig. 15.16 Schematic of a Stommel–Arons circulation in a two-hemisphere basin. There is only one mass source, and this is in the Southern Hemisphere and for convenience it has a strength of 2. Although there is no source in the Northern Hemisphere, there is still a western boundary current and a recirculation. The integrated sinks due to upwelling exactly match the strength of the source.

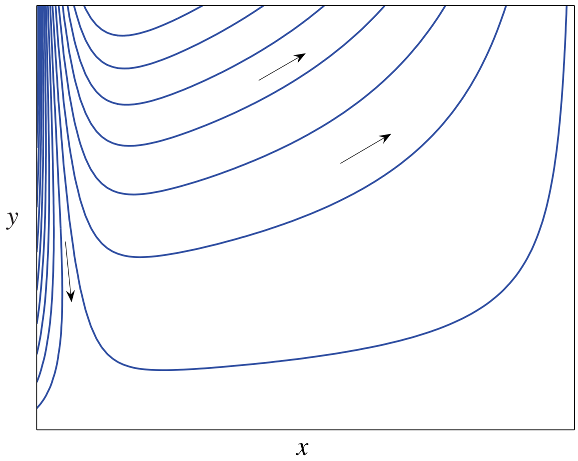

Fig. 15.17 The pressure field Φ for the shallow water Stommel–Arons model, as given by (15.102) with $r/\beta = 0.04x_E$, $f = \beta y$ and $y = 0$ at the equatorwards edge of the domain. The arrows indicate the flow direction, with the western boundary current diminishing in intensity as it moves equatorwards. The convective mass source is, implicitly, just polewards of the domain. (Note that the pressure field is not exactly a streamline.)

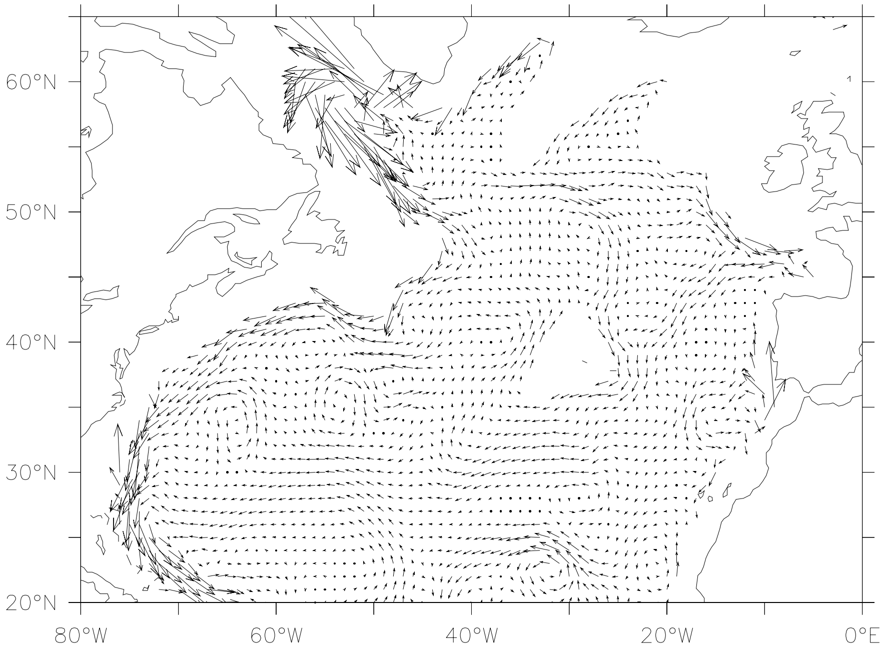

Fig. 15.18 The ocean currents at a depth of $2500\,\mathrm{m}$ in the North Atlantic, obtained using a combination of observations and model (as in Fig. 14.2). Note the southwards flowing *deep western boundary current.*

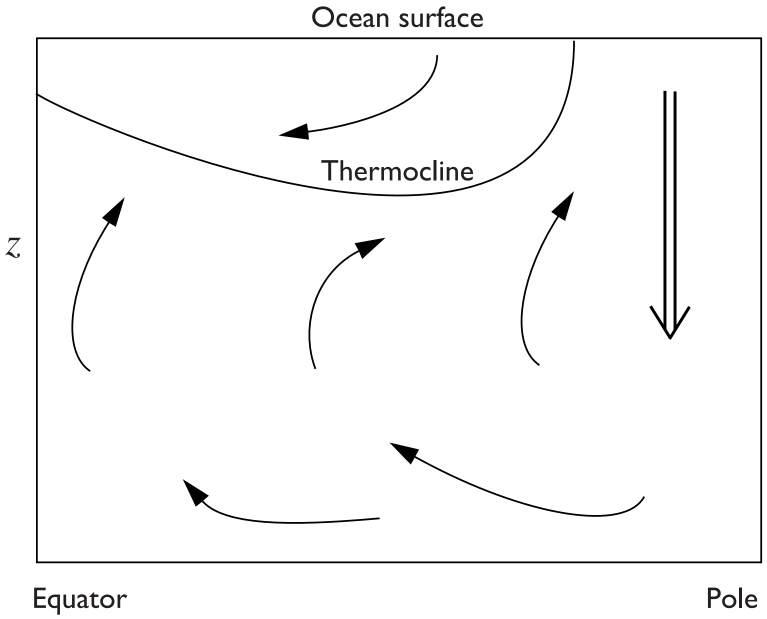

Fig. 16.1 Cartoon of a single-celled meridional overturning circulation. Sinking is concentrated at high latitudes and upwelling spread out over lower latitudes. The thermocline is the boundary between the cold abyssal waters, with polar origins, and the warmer near-surface subtropical water. Wind forcing in the subtropical gyre mechanically pushes the warm water down, increasing the depth of the thermocline.

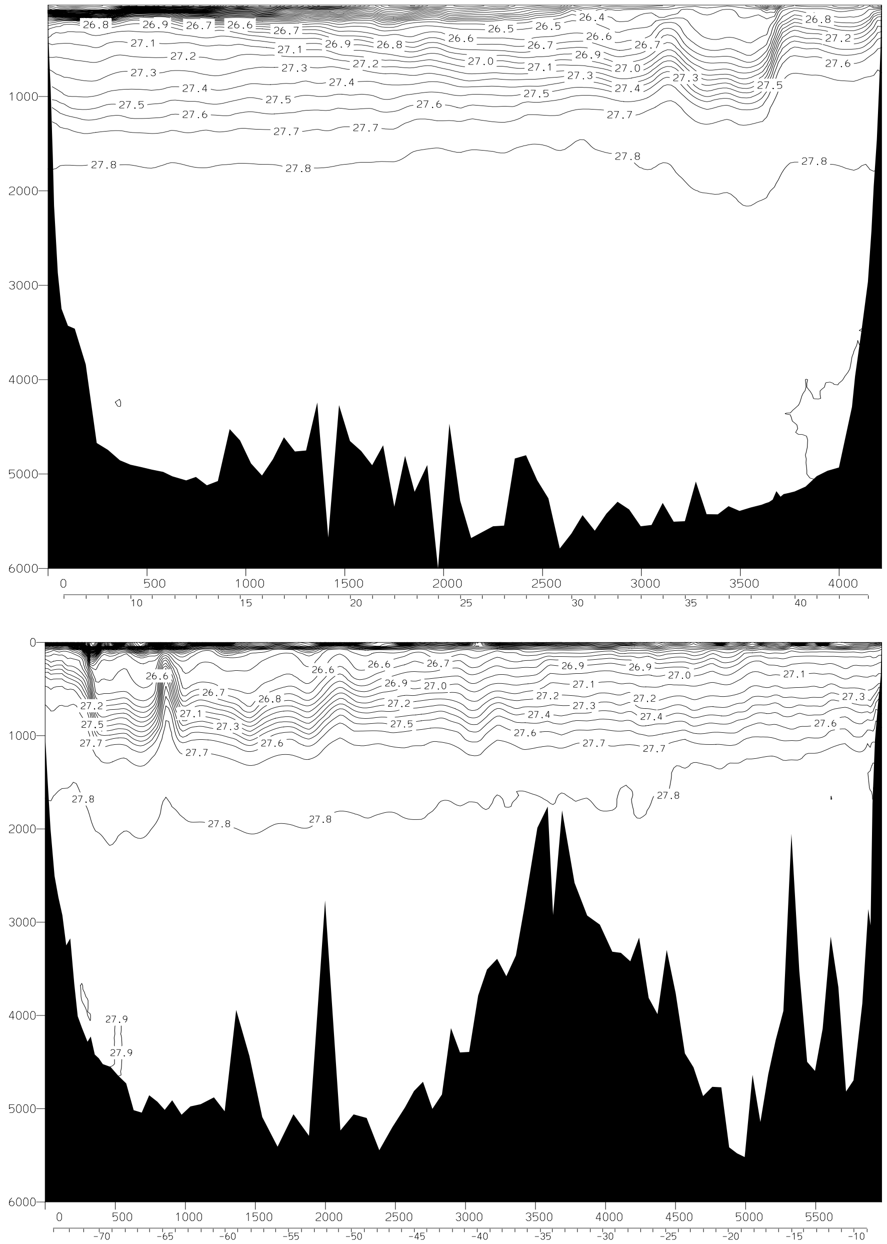

Fig. 16.2 Sections of potential density (σ_θ) in the North Atlantic. Upper panel: meridional section at 53°W, from 5°N to 45°N, across the subtropical gyre. Lower panel: zonal section at 36°N, from about 75°W to 10°W. A front is associated with the western boundary current and its departure from the coast near 40°N. In the upper northwestern region of the subtropical thermocline there is a region of low stratification known as MODE water: isopycnals above this outcrop in the subtropical gyre and are 'ventilated'; isopycnals below the MODE water outcrop in the subpolar gyre or ACC.[1]

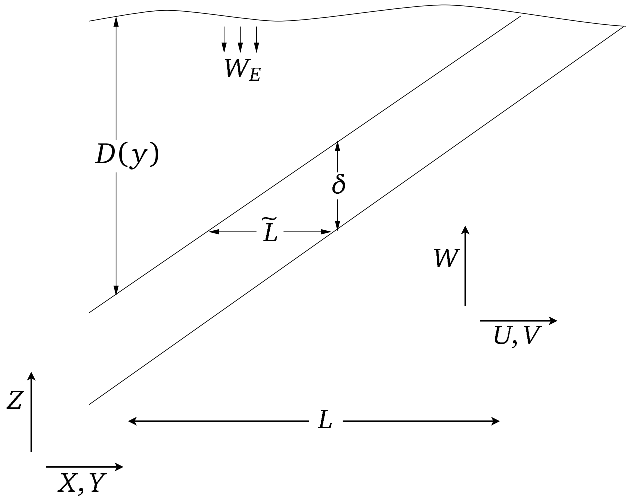

Fig. 16.3 Scaling the thermocline. The diagonal lines mark the diffusive thermocline of thickness δ and depth $D(y)$. The advective scaling for $D(y)$, i.e., D_a, is given by (16.8), and the diffusive scaling for δ is given by (16.13).

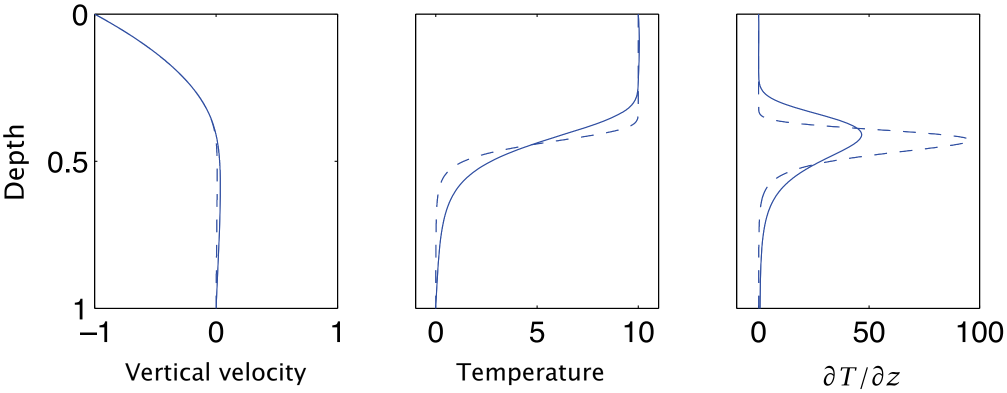

Fig. 16.4 Solution of the one-dimensional thermocline equation, (16.27), with boundary conditions (16.28), for two different values of the diffusivity: $\widehat{\kappa} = 3.2\times 10^{-3}$ (solid line) and $\widehat{\kappa} = 0.4\times 10^{-3}$ (dashed line), in the domain $0 \le \widehat{z} \le -1$. 'Vertical velocity' is W, 'temperature' is $-W_{\widehat{z}\widehat{z}}$, and all units are the non-dimensional ones of the equation itself. A negative vertical velocity, $\widehat{W}_E = -1$, is imposed at the surface (representing Ekman pumping) and $B_0 = 10$. The internal boundary layer thickness increases as $\widehat{\kappa}^{1/3}$, so doubling in thickness for an eightfold increase in $\widehat{\kappa}$. The upwelling velocity also increases with $\widehat{\kappa}$ (as $\widehat{\kappa}^{2/3}$), but this is barely noticeable on the graph because the downwelling velocity, above the internal boundary layer, is much larger and almost independent of $\widehat{\kappa}$. The depth of the boundary layer increases as $\widehat{W}_E^{1/2}$, so if $\widehat{W}_E = 0$ the boundary layer is at the surface, as in Fig. 16.5.

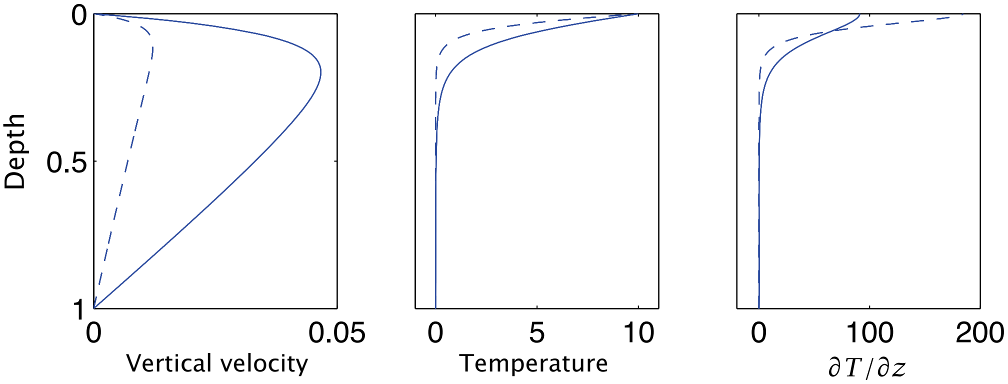

Fig. 16.5 As for Fig. 16.4, but with no imposed Ekman pumping velocity at the upper boundary ($\widehat{W_E} = 0$), again for two different values of the diffusivity: $\hat{\kappa} = 3.2 \times 10^{-3}$ (solid line) and $\hat{\kappa} = 0.4 \times 10^{-3}$ (dashed line). The boundary layer now forms at the upper surface. The boundary thickness again increases with diffusivity and, even more noticeably, so does the upwelling velocity — this scales as $\hat{\kappa}^{2/3}$, and so increases fourfold for an eightfold increase in $\hat{\kappa}$.

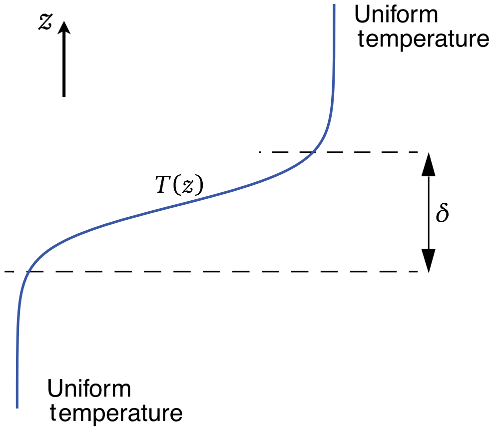

Fig. 16.6 The simplified boundary-layer structure of the internal thermocline. In the limit of small diffusivity the internal thermocline forms a boundary layer, of thickness δ in the figure, in which the temperature and buoyancy change rapidly.

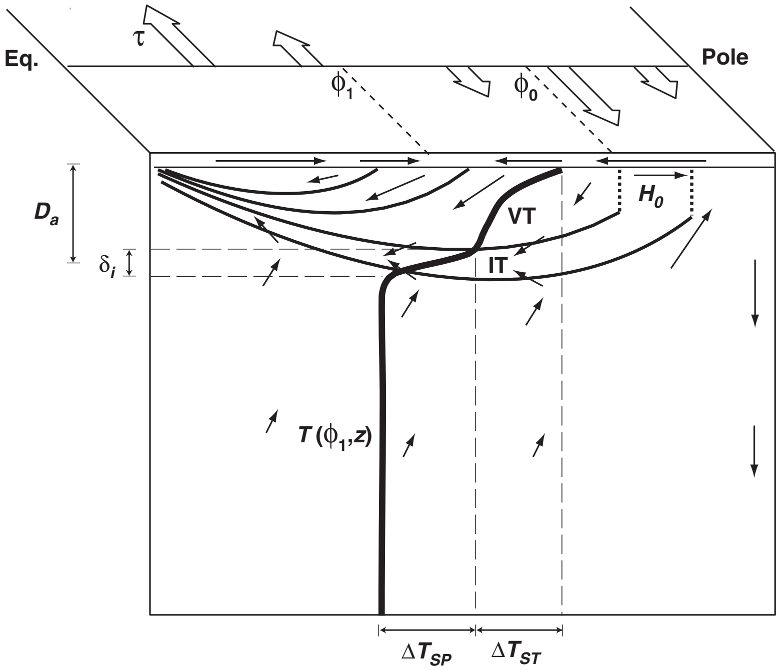

Fig. 16.7 Schema of the large-scale circulation and structure of the main thermocline, in a single-hemisphere ocean driven by wind stress (broad arrows) and a meridional gradient of heating at the surface. The subtropical–subpolar gyre boundary is a constant latitude ϕ_0, where the wind-stress curl changes sign. 'VT' denotes the ventilated thermocline, an advective regime of thickness D_a, and 'IT' denotes the internal thermocline, a diffusive internal boundary layer of thickness δ_I. The thin arrows indicate the meridional overturning circulation and the flow in the Ekman layer near the ocean surface. The thick line is a temperature profile at latitude ϕ_1: the temperature drop across the internal thermocline is ΔT_{SP}, equal to the meridional temperature difference across the subpolar gyre; the temperature drop across the ventilated thermocline is ΔT_{ST}, the temperature difference across the subtropical gyre.[2]

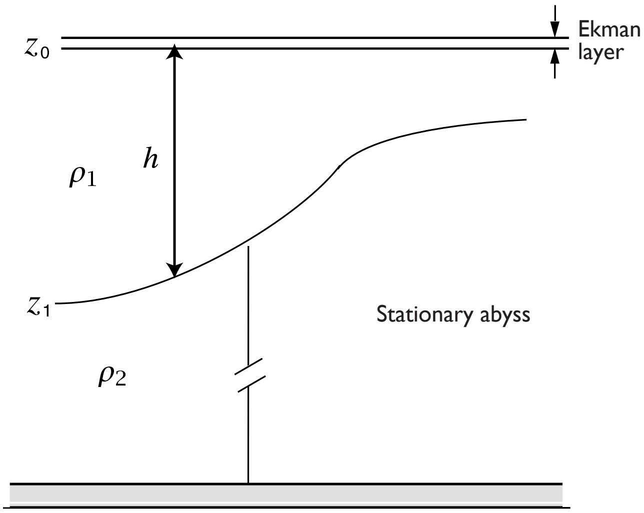

Fig. 16.8 A reduced gravity, single-layer model. A single moving layer lies above a deep, stationary layer of higher density. The upper surface is rigid. A thin Ekman layer may be envisioned to lie on top of the moving layer, providing a vertical velocity boundary condition.

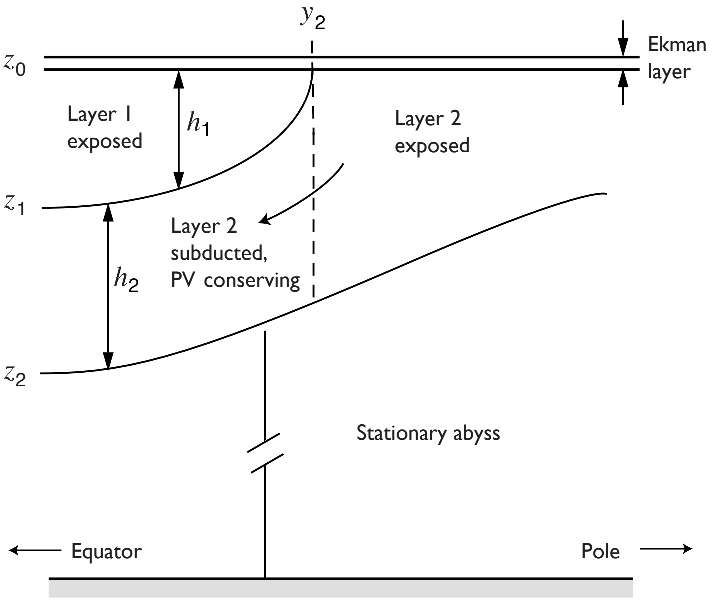

Fig. 16.9 A two-layer model of the ventilated thermocline. Two moving layers lie above an infinitely deep, stationary layer of higher density. Models with more moving layers may be constructed by straightforward extension.

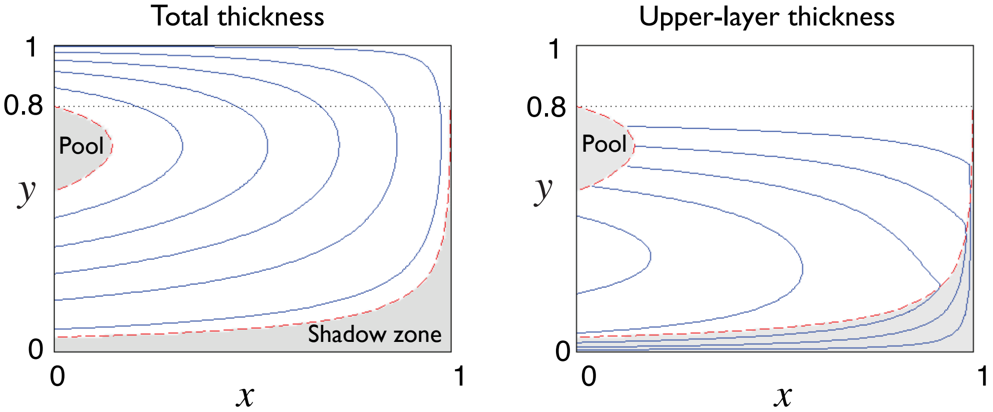

Fig. 16.10 Contour plots of total thickness and upper layer thickness in a two-layer model of the ventilated thermocline. The thickness generally increases westward, and the flow is clockwise. The shadow zone and the western pool are shaded, and no contours are drawn in the latter. The outcrop latitude, $y_2 = 0.8$, is marked with a dotted line. [Parameters are $g'_1 = g'_2 = 1$, $\beta = 1$, $f_0 = 0.5$, $H_e = 0.5$, and $w_E = -\sin(\pi y)$.]

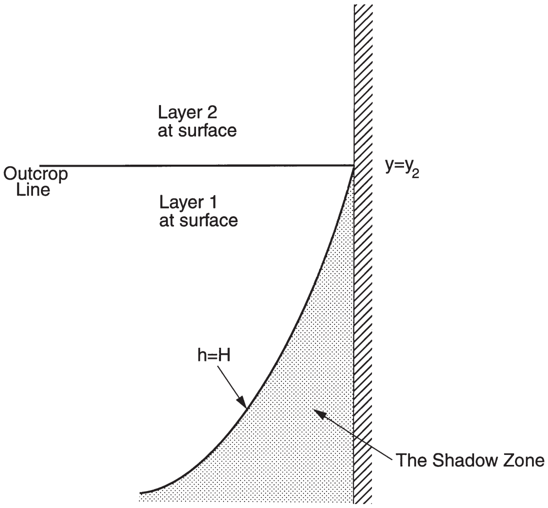

Fig. 16.11 The shadow zone in the ventilated thermocline. Layer 2 outcrops at $y = y_2$. A column moving equatorwards along the eastern boundary in layer 2 is subducted at y_2. It cannot remain against the eastern wall and both preserve its potential vorticity, which implies the column shrinks, at the same time that the no-normal flow condition is satisfied, as by geostrophy this implies the layer depth is constant. Thus, the column must move westward, along the boundary of a 'shadow zone' within which there is no motion. The streamline it follows is the isoline of constant total thickness of the two moving layers [see (16.120) or (16.122c)].

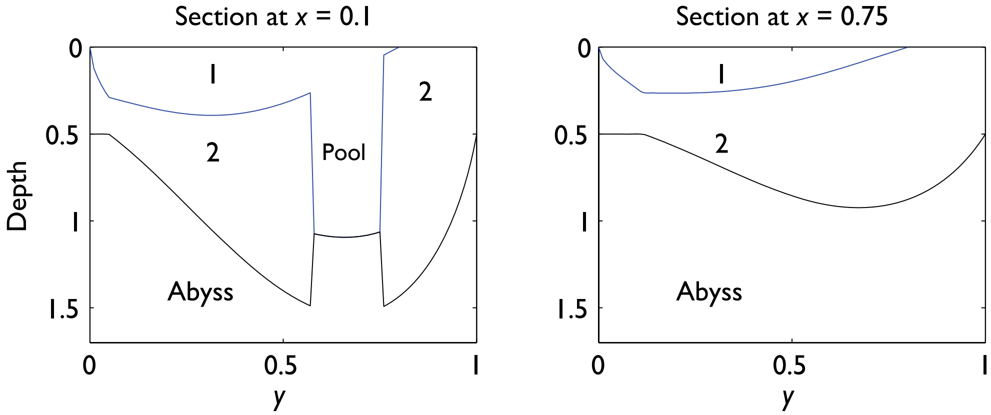

Fig. 16.12 Two north-south section of layer thickness, at different longitudes, from the same solution as Fig. 16.10 and assuming a ventilated western pool. The numbers refer to the fluid layer. The section on the left passes through the western ventilated pool region, where all the Sverdrup transport is taken up by the top layer. The region near $y = 0$ in both plots where the total depth of the thermocline is constant is the shadow zone.

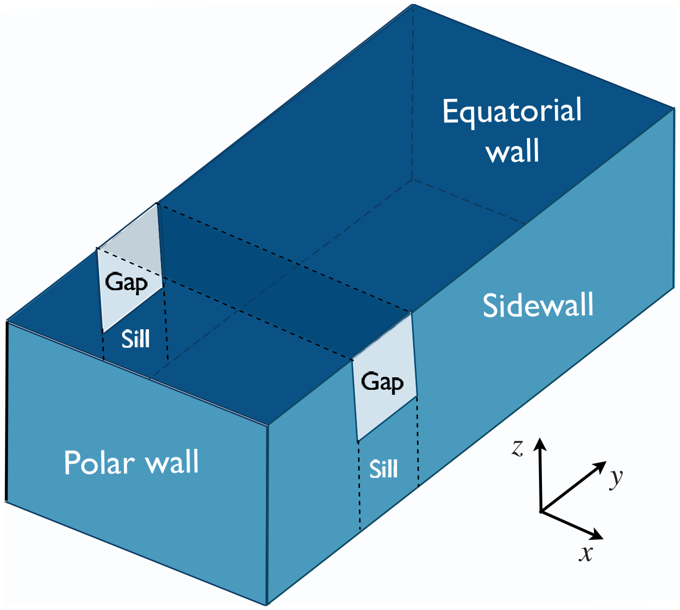

Fig. 16.13 Idealized geometry of the Southern Ocean: a re-entrant channel, partially blocked by a sill, is embedded within a closed rectangular basin; thus, the channel has periodic boundary conditions, whereas elsewhere there is no normal flow. The channel is a crude model of the Antarctic Circumpolar Current, with the area over the sill analagous to the Drake Passage.

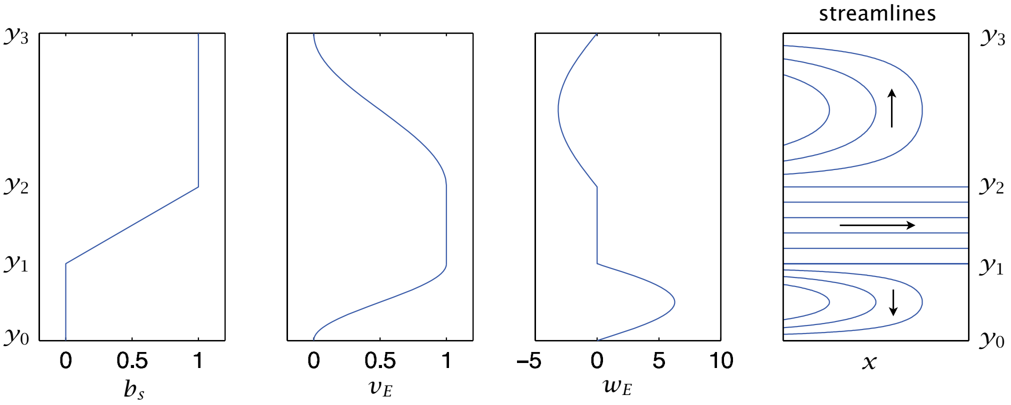

Fig. 16.14 The surface buoyancy b_s, merdional Ekman velocity v_E, vertical Ekman velocity w_E and the solution streamlines for the geostrophic horizontal flow, omitting the western boundary currents. The ordinate in all plots is latitude, with the pole at the bottom, and the four fields are given by, respectively, (16.73), (16.74a), (16.74b) and (16.75), with purely zonal flow given by (16.78) in the channel.

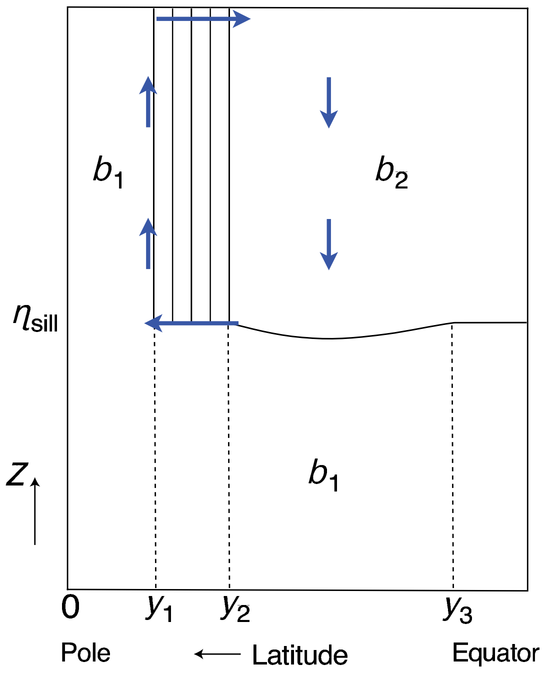

Fig. 16.15 Cross-section of the structure of the single-hemisphere ocean model described in section 16.5.1. The domain is zonally closed equatorwards of y_2 and polewards of y_1, with a zonally periodic channel between latitudes y_1 and y_2 and above the sill, which has height η_{sill}. The arrows indicate the fluid flow driven by the equatorwards Ekman transport in the channel, and the solid lines are isopycnals.

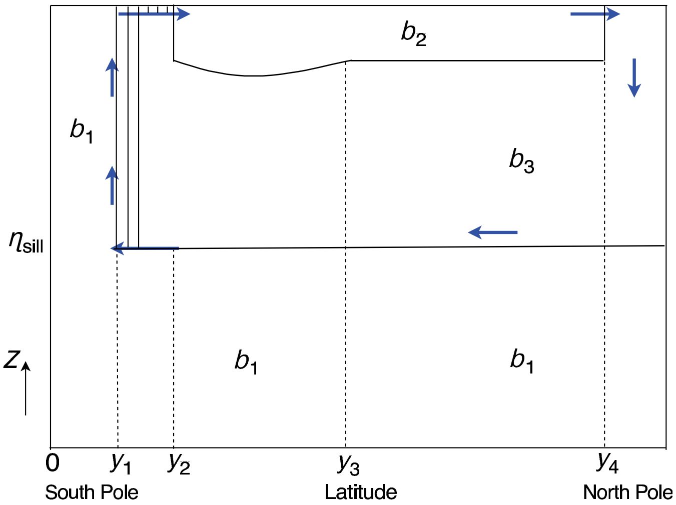

Fig. 16.16 As for Fig. 16.15, but now for a two-hemisphere ocean with a source of dense water, b_3, at high northern latitudes. The solid lines are isopycnals, and here the wind is zero in the Northern Hemisphere.

From Vallis (2006)

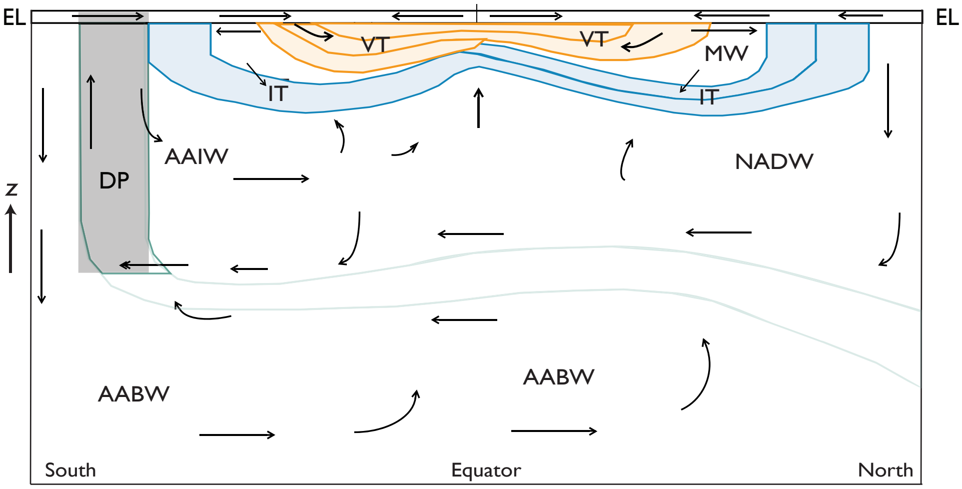

Fig. 16.17 A schema of the stratification and overturning circulation obtained by combining the thermocline models of sections 16.1–16.4 with the model of deep overturning of section 16.5. Key: DP – Drake Passage; EL – Ekman layer; VT – ventilated thermocline; IT – internal thermocline; AABW – Antarctic Bottom Water; AAIW – Antarctic Intermediate Water; NADW – North Atlantic Deep Water: MW – Mode Water. The shaded regions mark the main regions of stratification and the Drake Passage. The real ocean is more complex; see text.

From Vallis (2006)

From Vallis (2006)

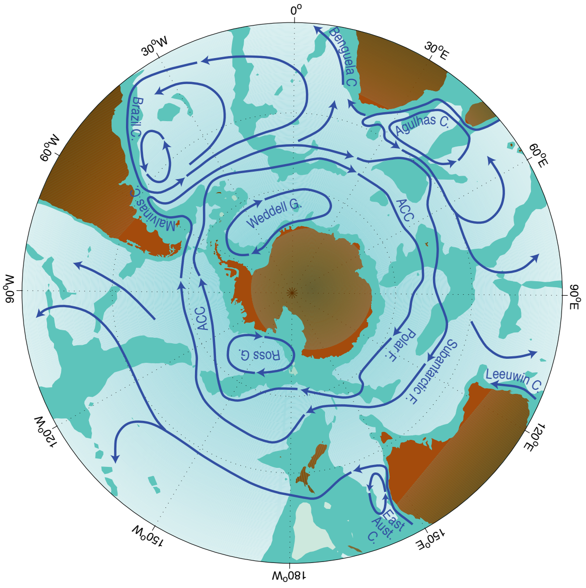

Fig. 16.18 Schema of the major currents in the Southern Ocean. Shown are the South Atlantic subtropic gyre, and the two main cores of the ACC, associated with the Polar front and the sub-Antarctic front.[3]

From Vallis (2006)

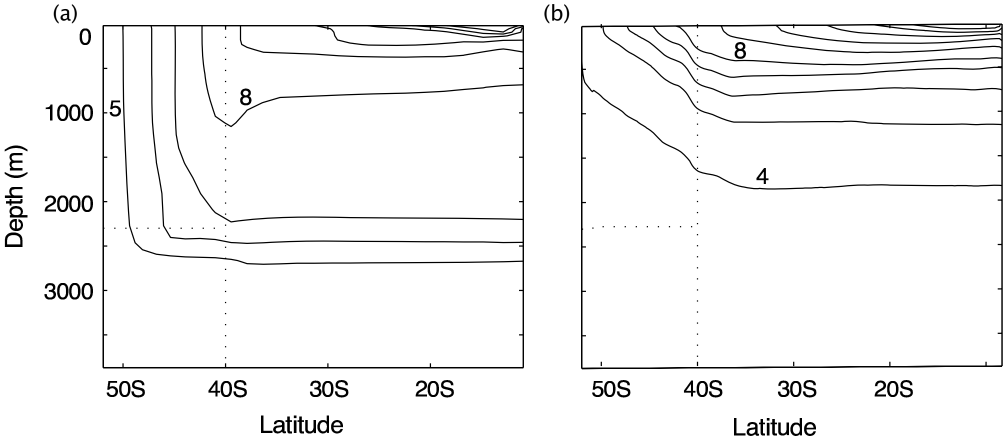

Fig. 16.19 The zonally averaged temperature field in numerical solutions of the primitive equations in a domain similar to that of Fig. 16.13 (except that here the channel and sill are nestled against the polewards boundary). Panel (a) shows the steady solution of a diffusive model with no baroclinic eddies, and (b) shows the time averaged solution in a higher-resolution model that allows baroclinic eddies to develop. Two contour values in each panel are labelled. The dotted lines show the channel boundaries and the sill.[4]

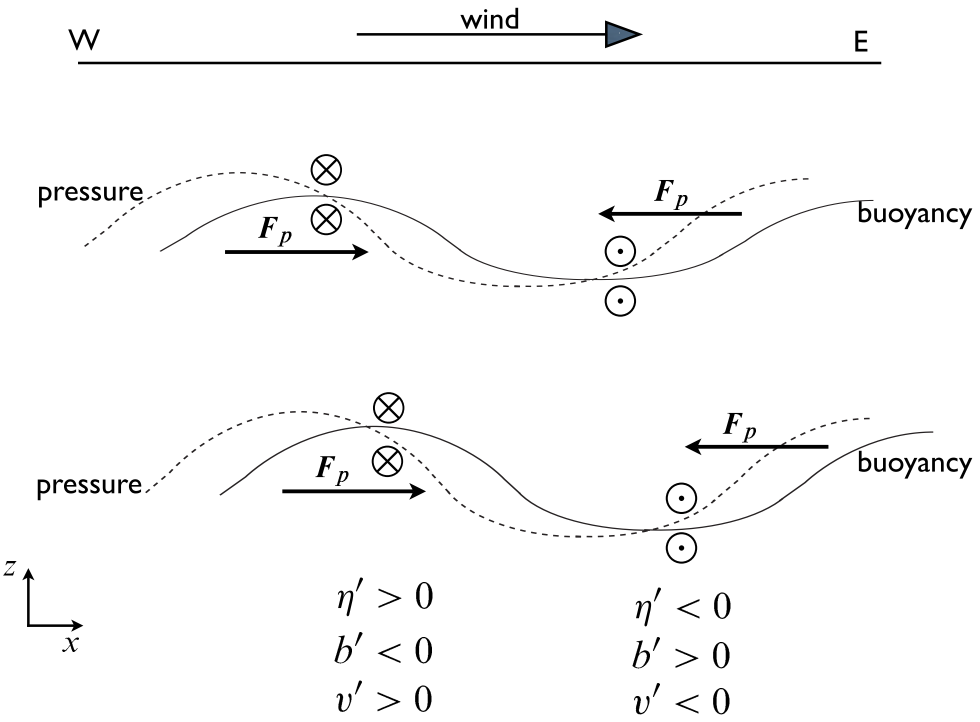

Fig. 16.20 Eddy fluxes and form drag in a Southern Hemisphere channel, viewed from the south. In this example, cold (less buoyant) water flows equatorwards and warm water polewards, so that $\overline{v'b'} < 0$. The pressure field associated with this flow (dashed lines) provides a form drag on the successive layers, $\boldsymbol{F}_p$, shown. At the ocean bottom the westward form drag on the fluid arising through its interaction with the orography of the sea-floor is equal and opposite to that of the eastward wind stress at the top. The mass fluxes in each layer are given by $\overline{v'h'} \approx -\partial_z(\overline{v'b'}/N^2)$. If the magnitude of buoyancy displacement increases with depth then $\overline{v'h'} < 0$.

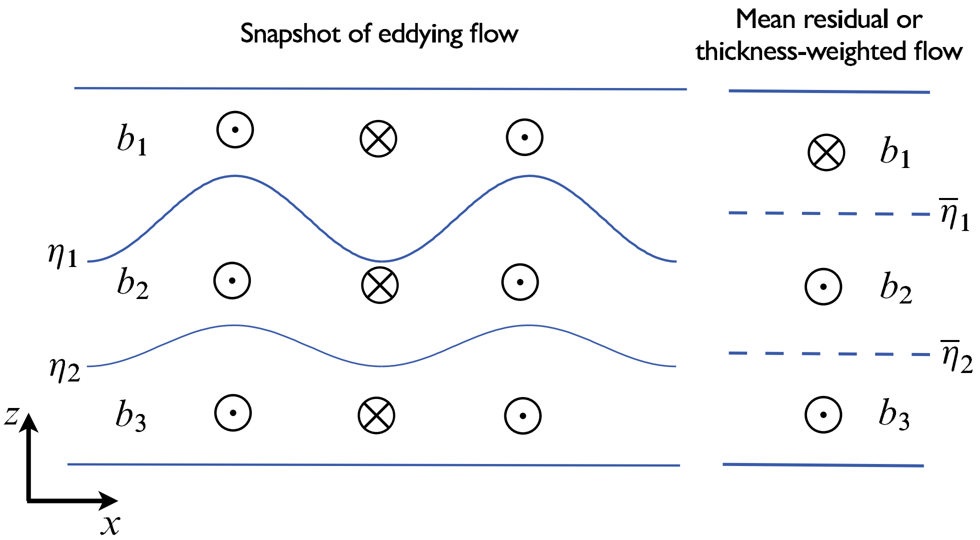

Fig. 16.21 An example of the meridional flow in an eddying channel. The eddying flow may be organized such that, even though at any given level the Eulerian meridional flow may be small, there is a net flow in a given isopycnal layer. The residual ($\overline{v}^*$) and Eulerian ($\overline{v}$) flows are related by $\overline{v}^* = \overline{v} + \overline{v'h'}/\overline{h}$; thus, the thickness-weighted average of the eddying flow on the left gives rise to the residual flow on the right, where $\overline{\eta}_i$ denotes the mean elevation of the isopycnal interface η_i.

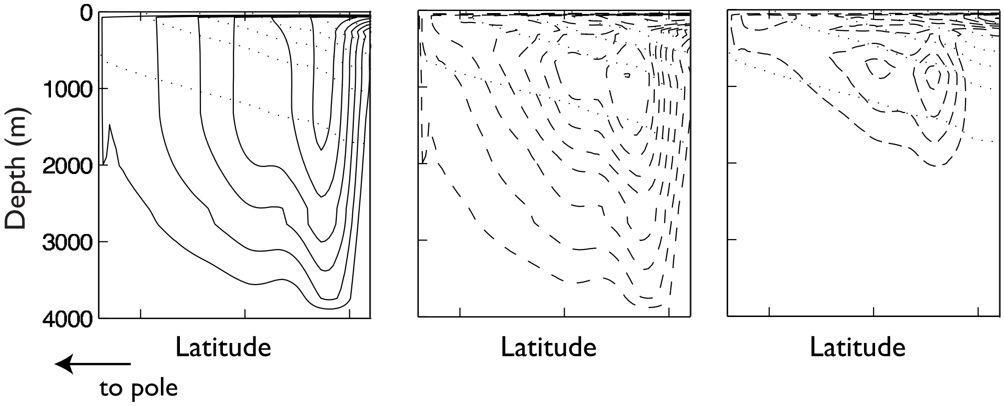

Fig. 16.22 The meridional circulation in the re-entrant channel of an idealized, eddying numerical model of the ACC (as in Fig. 16.19, but showing only the region south of 40°S). Left panel, the zonally averaged Eulerian circulation. Middle panel, the eddy-induced circulation. Right panel, the residual circulation. Solid lines represent a clockwise circulation and dashed lines represent anticlockwise circulation. The faint dotted lines are the mean isopycnals. The overturning circulation of the ACC is called the Deacon Cell.

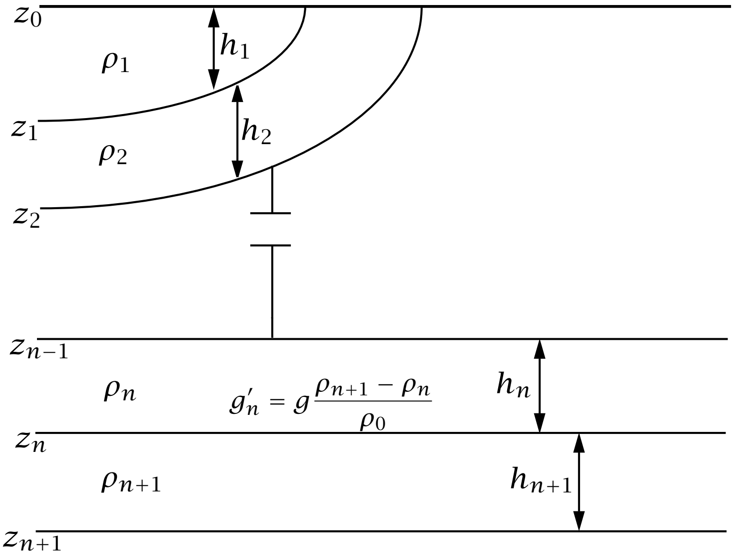

Fig. 16.23 Structure and notational conventions used for a multi-layered model.